On Residual Stress Analysis and Microstructural Evolution for Stainless Steel Type 304 Spent Nuclear Fuel Canisters Weld Joint: Numerical and Experimental Studies

Xin Wu

George S. Ansell Department of Metallurgical and Materials Engineering, Colorado School of Mines, Golden, CO 80401

Email address: xinwu350@gmail.com

ABSTRACT

Chloride-induced stress corrosion cracking (CISCC) in the weldments of austenitic stainless steel canisters is one of the primary safety concerns during the dry storage of used nuclear fuel at Independent Spent Fuel Storage Installations in coastal areas. In order to evaluate the CISCC behavior in the canister, a 3D sequentially coupled thermo-mechanical finite element model was built to simulate the residual stresses induced by two intersecting longitudinal and circumferential multi-pass welds in austenitic stainless steel mockup canister. Weld-induced residual stresses from simulation were in good agreement with the experimental measurement results by deep-hole drilling and contour methods. Through-wall high tensile axial and hoop stresses were observed in both the fusion zone and heat affected zone (HAZ) in the longitudinal and circumferential weld, respectively. On the other hand, the microstructure within the weldments of 304 stainless steel mockup was characterized using optical microscopy, scanning electron microscopy, electron back-scattered diffraction and energy dispersive X-ray spectroscopy methods. A few amount of MnS inclusions in both the base metal and HAZ, and a lot of $(Mn,Si)_xO_y$ inclusions in the fusion zone were found. Meanwhile, there is some α'-martensite in the base metal, while the martensite was reversed in the HAZ. In the fusion zone, there is a lot of δ-ferrite. The martensite reversion phenomenon was also verified by the combination of Feritscope test and thermal simulation, which could predict a martensite reversion temperature as 400C°. The welding residual stresses and microstructure analysis results could offer the instructive information for the prediction of CISCC behavior of the spent nuclear fuel canisters.

Keywords: Stress corrosion cracking; Spent nuclear fuel canister; Welding residual stress; Finite element simulation; Microstructure

1. Introduction

Before the final disposal, the spent nuclear fuel (SNF) is generally stored in the helium-filled stainless steel canisters of dry storage system [1]. As a result of several recent decisions, such as not pursuing Yucca Mountain as a long-term geologic repository storage facility for SNF and the cancellation of the construction of a reprocessing facility in the 1980s due to proliferation risks, interim dry storage facilities for long-term storage are vital for the immediate future of nuclear energy technology. Lifetime extension of dry storage canisters requires thorough understanding of the behavior of the canister material in corrosive environment and stressed conditions and the ability to accurately predict and monitor material degradation so that corrective maintenance actions can be taken. Chloride-induced stress

corrosion cracking (CISCC) in the weldments of SNF canisters is one of the primary safety concerns during the dry storage of used nuclear fuel at Independent Spent Fuel Storage Installations (ISFSI) in coastal areas [2]. CISCC has been proved to be able to lead to through-wall failures in the weld heat affected zone (HAZ) of interim storage containers [3].

For SCC to occur, three criteria must be met: an aggressive chemical environment, susceptible microstructure, and sufficient tensile stress. Field sampling analysis of surface deposits on in-service SNF storage canisters at three near-marine ISFSI sites in the United States have demonstrated the presence of chloride-rich salts on the canister surfaces [4-6]. As canister surface locations cool sufficiently for the salts to deliquesce, a chloride-rich brine could form locally on the surface providing the required aggressive surface environment. Moreover, the multi-pass welding procedure used for the austenitic stainless steel SNF interim canisters introduces high through-wall tensile residual stresses [3-6], and also introduces microstructural changes (sensitization) in the HAZ that increase metal susceptibility to corrosion. The combination of these factors can lead to potential through-wall failures by CISCC in the weldments of the stainless steel interim storage canisters.

To gain a fundamental understanding of the pitting and cracking behavior in the canisters and accurately predict their long-term performance, the first step is to obtain the residual stress distribution within the canisters, especially in the weldments. Different techniques, including neutron diffraction, contour method, hole drilling, numerical methods, have been successfully applied in obtaining the residual stresses in a weldment [7-10]. In the last decade, there have been several studies on the residual stress in the canister welds. For example, Kosaki et al. [11] reported that the experimentally measured maximum residual stress was close to the yield point on a cylindrical canister of 1.3m in diameter and ~75mm in thickness. Kusnick et al. [12] simulated the residual stresses for typical canister welds by employing a two-dimensional sequentially coupled thermal-structural finite element (FE) model, and predicted that tensile stresses of sufficient magnitude to initiate SCC are likely to present in the HAZ of both longitudinal and circumferential welds through the wall thickness of the canisters, allowing for crack propagation through the wall thickness over time. By using neutron diffraction method, Wang et al. [13] has demonstrated a throughout thickness high tensile residual stress of the weldment in the fusion zone and part of the HAZ for the 304L SS canister, for which the stress profiles agree with the data from deep hole drilling approach [14]. To relieve the large tensile residual stresses in the canister weldment, gas-tungsten arc repaired welding method [15] and laser peening [16] method were proposed, and the compressive residual stresses could even be generated for the treated samples. However, there is very limited literature on 3D simulation of the residual stress induced by multi-pass longitudinal and circumferential welds in the dry storage canisters. Besides, we couldn't find any comparisons between the experimental test and simulation results relevant to the welding residual stress of the canisters. As for the microstructure of the canister material, the possible factors that may influence the CISCC include the sensitization, ferrite, martensite, inclusions, grain size, phase orientation, texture, and so on. It was demonstrated that SCC could occur in stainless steel pipes due to the sensitizing of region in the HAZ [17]. The sensitization can induce the chrome depletion at grain boundaries due to the precipitation of chromium

carbides. What's more, the high density of quasi martensite induced by cold working could result in higher SCC susceptibility as dissolution rate of martensite in the corrosive environment is higher than austenite [18]. There have been many researchers studied the influence of microstructure on the SCC of stainless steel, while due to the difficulties in conducting the measurement, few reports can be found discussing the SCC behavior for in-service canister under the consideration of microstructure. The segments of published papers and theoretical articles show the shortage of the in-service canisters.

This paper will focus on the weld residual stress and susceptible macrostructure factors, which could contribute to the database of the CISCC prediction for the SNF canister. First, a full-diameter cylindrical mockup of an interim storage canister was produced using the same manufacturing procedures as the majority of the fielded SNF interim storage canisters, and the weld residual stresses of the mockup canister were measured by experimental methods. The details for the construction of the mockup and the residual stress measurement should be referred to Ref. [14]. Then, based on the actual weld parameters and geometry of the mockup, a 3D FE model using ABAQUS software was built to simulate the residual stresses in the type 304 stainless steel canisters with the presence of both the longitudinal and circumferential multi-pass welds. The simulated residual stresses were compared to the experimental data. Besides, the microstructures of the different regions in the mockup were characterized using optical microscopy, scanning electron microscopy, electron back-scattered diffraction, energy dispersive X-ray spectroscopy and Feritscope methods. The potential SCC behavior of the mockup canister was finally discussed on the basis of the obtained residual stress and microstructure results.

2. Experiment and simulation details

2.1 Experimental procedures

As depicted in Fig. 1(a), the mockup consists of three cylindrical shells that were 3660mm (12 feet) long and 15.9mm (5/8 inch) thick. The shells were rolled from plate into a cylinder and then welded at the longitudinal seam. The three cylinders were then welded together using two circumferential welds. All of the welds were formed via the submerged-arc welding process and were multi-pass. The plates were constituted by dual certified 304/304L stainless steel (SS) and the weld filler metal was 308L SS, as typically used when welding 304 SS. The compositions of the 304/304L SS plates and the 308L SS filler material are shown in Table 1 below. Details of the welding parameters including pass sequence, voltage, current, travel speed and heat input for each weld pass are listed in Table 2. After the welding process, the mockup was cut into small parts for various characterizations. Fig. 1(b) gives the weld bead morphology for each pass in the circumferential and longitudinal weld. It clearly shows the seven passes for the longitudinal weld and eight passes for the circumferential weld. Deep-hole drilling (DHD) and contour methods were then adopted to characterize the weld residual stresses on the mockup canister, as described in Ref. [14].

To observe the microstructure under the optical and electron microscope, specimens were cut from different zones of the mockup, i.e, base metal (BM), HAZ, and weld metal

(WM), and then prepared according to the standard procedures. The overall distribution of the inclusions in each region was analyzed using an Olympus PMG-3 microscope fitted with a PAXcam with PAX-It version 7.8.1.0 image capture and analysis software. An FEI Quanta 600i environmental scanning electron microscope (ESEM) with Quanta xT operating software was used to examine the morphology of the microstructures in different zones. An aqueous solution HCl:HNO_3 (3:1) was used to etch the SEM specimens for around 15s. Energy dispersive X-ray spectroscopy (EDS) was conducted on a JEOL JSM-7000F field emission SEM (FESEM) with JEOL PC-SEM7000 operating software and Genesis Spectrum 6.5 EDS collection software to characterize the inclusions composition in different regions. Spot scanning mode was performed for base matrix and the inclusions with a dwell time of more than 30s for the EDS analysis. Electron backscatter diffraction (EBSD) patterns for bcc ferrite and fcc austenite were collected using an EDAX AMETEK 9424 detector and TSL-OIM Data collection 7 software with a working distance of 21mm 4x4 binning was used, gain was adjusted to 2.4-2.8 and exposure was increased to just before the evolution of blurry white spots. For surface preparation, vibratory polishing was performed using a Beuhler Vibromet 2 before EBSD work. The typical step size used for the EBSD test was 0.1μm. For each location, three EBSD test samples has been prepared and the phase fraction values were averaged. The content of δ-ferrite in the WM and δ-ferrite/α'-martensite in the BM was determined with a Fischer Feritscope FMP30 axial single tip probe with spring loaded measuring system. The Feritscope uses the magnetic property to estimate the quantity. Therefore, all magnetizable structures can be measured (δ-ferrite, α'-martensite and other ferritic phases) through this method. The α'-martensite in the BM was generated due to cold forming process of the mockup canister. The ferrite number (FN) data from the Feritscope test is almost equal to the ferrite volume fraction when FN is small [19].

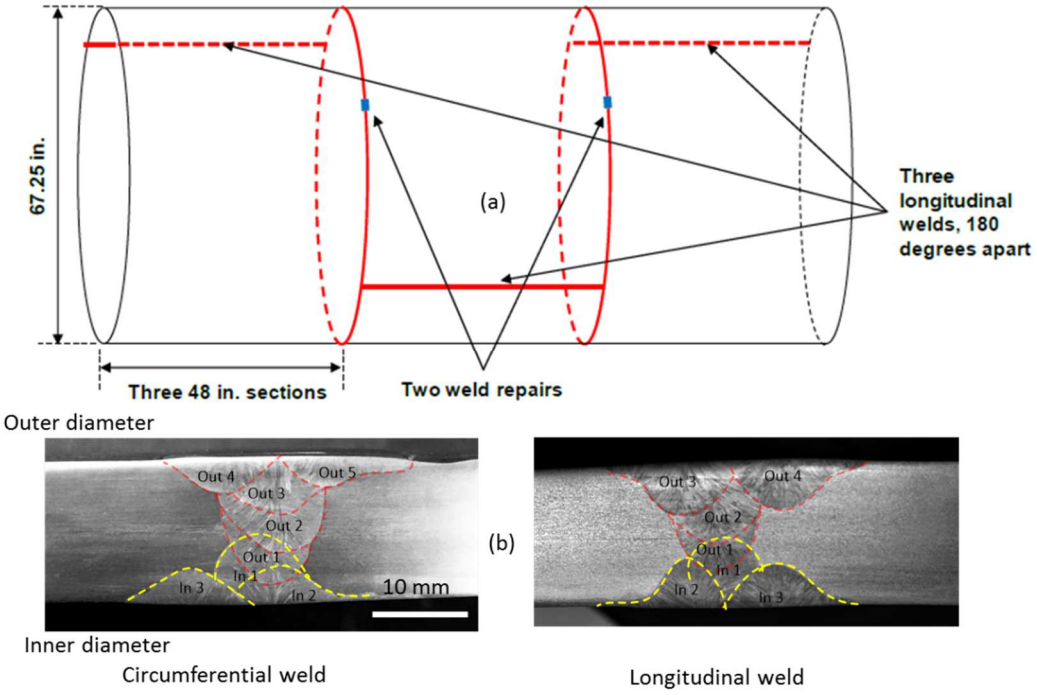

Fig. 1. (a) Schematic drawing of the mockup and (b) the corresponding weld bead morphology for each pass

[键入文字]

Table 1 Composition of 304/304L plate and 308L filler metal used to construct the mockup canister (wt.%)

Materials	C	Co	Cr	Cu	Mn	Mo	N	Ni	P	S	Si
Plate Material (304/304L)	0.0223	0.1865	18.100	0.4225	1.7125	0.3180	0.0787	8.0270	0.0305	0.0023	0.2560
Weld Filler (308L) (lot 1)	0.014	-	19.66	0.16	1.70	0.11	0.058	9.56	0.025	0.010	0.39
Weld Filler (308L) (lot 2)	0.012	-	19.71	0.192	1.730	0.071	0.053	9.750	0.024	0.012	0.368

Table 2 Weld parameters of the mockup canister

Weld Joint 1 (WJ-1)		Longitudinal			
	Interpass temeprature	Amperage	Voltage	Travel Speed (IPM)	Heat Input
ID - Pass 1	74	400	30	15.4	46753
ID - Pass 2	199	400	30	15.42	46755
ID - Pass 3	214	400	30	15.4	46753
OD - Pass 1	69	400	30	15.16	47493
OD - Pass 2	104	400	30	15.16	47493
OD - Pass 3	110	400	30	15.16	47493
OD - Pass 4	177	400	30	15.16	47493
Weld Joint 2 (WJ-2)		Longitudinal			
	Interpass temeprature	Amperage	Voltage	Travel Speed (IPM)	Heat Input
ID - Pass 1	76	400	30	15.4	46753
ID - Pass 2	161	400	30	15.4	46753
ID - Pass 3	181	400	30	15.42	46755
OD - Pass 1	75	400	30	15.16	47493
OD - Pass 2	148	400	30	15.16	47493
OD - Pass 3	187	400	30	15.16	47493
OD - Pass 4	155	400	30	15.16	47493
Weld Joint 3 (WJ-3)		Longitudinal			
	Interpass temeprature	Amperage	Voltage	Travel Speed (IPM)	Heat Input
ID - Pass 1	76	400	30	15.48	46512
ID - Pass 2	161	400	30	15.4	46753
ID - Pass 3	181	400	30	15.4	46753
OD - Pass 1	75	400	30	15.16	47493
OD - Pass 2	123	400	30	15.16	47493
OD - Pass 3	122	400	30	15.16	47493
OD - Pass 4	210	400	30	15.16	47493
Weld Joint 4 (WJ-4)		Circumferential			
	Interpass temeprature	Amperage	Voltage	Travel Speed (IPM)	Heat Input
ID - Pass 1	70	400	30	16.4	43902
ID - Pass 2	199	400	30	16.4	43902
ID - Pass 3	214	400	30	16.4	43902
OD - Pass 1	74	400	30	15.8	45454
OD - Pass 2	85	400	30	15.8	45454
OD - Pass 3	110	400	30	15.8	45454
OD - Pass 4	88	400	30	15.8	45454
OD - Pass 5	97	400	30	15.8	45454
Weld Joint 5 (WJ-5)		Circumferential			
	Interpass temeprature	Amperage	Voltage	Travel Speed (IPM)	Heat Input
ID - Pass 1	77	400	30	16.4	43902
ID - Pass 2	126	400	30	16.4	43902
ID - Pass 3	135	400	30	16.4	43902
OD - Pass 1	68	400	30	15.1	47682
OD - Pass 2	102	400	30	15.1	47682
OD - Pass 3	176	400	30	15.1	47682
OD - Pass 4	160	400	30	15.73	45772

2.2 Simulation model

ABAQUS software was used to build the residual stress simulation models for longitudinal and circumferential double-V groove multi-pass welds. Fig. 2 demonstrates the meshed structure with 52100 brick elements established based on the actual geometry of the

mockup and the welding conditions as schematically illustrated in Fig. 1. The mockup consists of three cylindrical shells that were 3660mm (12 feet) long and 15.9mm (5/8 inch) thick as shown in Fig. 1(a). According to the actual welding procedures in the experiment, the weld simulation starts from the inner side to the outer side. Take longitudinal welds for example, the three inner passes were made first, followed by the four passes in outer diameters. Since the three longitudinal welds were arranged 180 degrees apart and the two circumferential welds were separated by the middle section, the interference between the same welding types can be negligible. Hence, in this finite element analysis (FEA) model, only the longitudinal and circumferential intersecting joint in half of the mockup section was simulated as shown in Fig. 2, and the welding length was sufficient to reach steady state. Note that the heat source traveled through the whole length of the welds to make sure the elements experience the same thermal history as the actual welds did. In the model, the nonlinear transient heat conduction analysis was performed first to get the temperature distribution during each welding pass. Then, the temperature history result was employed as a thermal body load in the subsequent non-linear mechanical elastic-plastic calculation to obtain the residual stress distribution. The model change option was used to simulate the weld metal deposition, which means during the first weld pass, the other weld pass elements were killed. After the first weld was finished, the elements for the second pass were made active to simulate the weld metal deposition into the groove. Similarly, during the longitudinal welding passes, the circumferential weld elements were not activated.

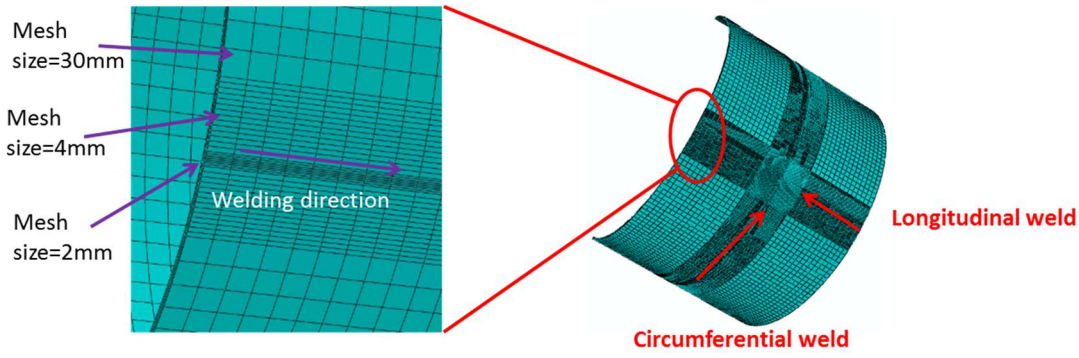

Fig. 2. The FEA model for the mockup with fine meshes near welds

The multi-pass weld beads have sharp transition angles, as shown in Fig. 1(b), which demands extremely fine meshes. More importantly, the intersecting longitudinal and circumferential welds need compatible meshing. Due to such complications, the weld bead was divided into small rectangle-shaped areas matching the experiment bead morphology as closely as possible. The experimental bead morphology of each pass is outlined by the dashed line in Fig. 3 and the corresponding simulation passes are highlighted in various colors. Such simplification avoided the elements with sharp angles and assisted the FE model to converge more easily.

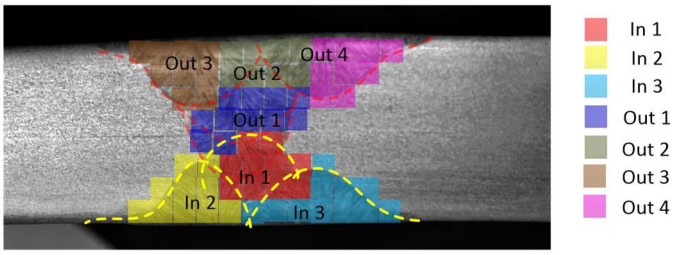

Fig. 3. Experimental bead morphology (longitudinal weld) and the corresponding computational weld bead

The mockup base material is 304 SS. The material properties used in the simulation were taken from Deng's work [20]. The temperature-dependent hardening modulus used in this model was obtained from Liu's work [21]. The material solidus and liquidus temperatures were set at 1450 and 1500℃, respectively. The latent heat of fusion was set to be 260kJ/kg. The material properties were assumed to be the same for both base and weld metals due to lack of information in 308 SS weld metal physical properties.

Double-ellipsoidal heat source model developed by Goldak [22] as illustrated in Fig. 4 was used to simulate the heat input of submerged-arc welding process. The front and rear parts of the heat flux are descried by Eqs. (1) and (2), respectively:

$$q_r(x,y,z) = \frac{6\sqrt{3} f_r \eta Q}{a_r bc\pi\sqrt{\pi}} \exp\left(-\frac{3x^2}{a_r^2} - \frac{3y^2}{b^2} - \frac{3z^2}{c^2}\right) \quad (1)$$

$$q_f(x,y,z) = \frac{6\sqrt{3} f_f \eta Q}{a_f bc\pi\sqrt{\pi}} \exp\left(-\frac{3x^2}{a_f^2} - \frac{3y^2}{b^2} - \frac{3z^2}{c^2}\right) \quad (2)$$

where the front and rear quadrant fractions, f_f and f_r, were set to be 0.6 and 1.4, respectively. The heat input was defined as $Q=V*I*\eta$, where V=30V, I=400A and η=0.8. a_f, a_r, b, c were set to be 13, 26, 13, 13, respectively, to closely match the experimental fusion boundary in Fig. 1(b).

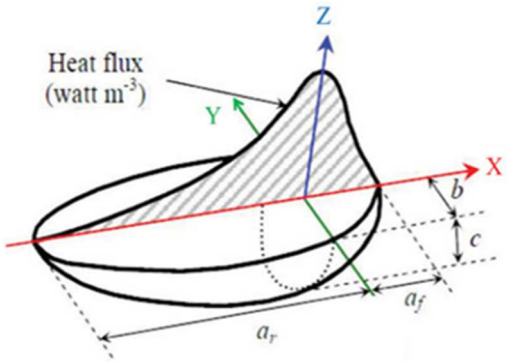

Fig. 4. Heat source model used for weld simulation [22].

3. Results

3.1 Temperature profiles in weldments

The constants (a_f, a_r, b, c) in Eqs. (1)-(2) were adjusted to match the fusion boundary of the experimental welds. The fusion zone generated from the three inner passes and four outer passes of the longitudinal welds were integrated to calculate an overall fusion boundary for the whole welding process, as depicted in Fig. 5. Fig. 5(c) compares the integrated fusion boundary to the experimentally observed of the longitudinal welds. The good match between the simulated and the measured molten pool demonstrates the rationality of the FEA model. Of course, there exists some deviations between the experimental characterization and the simulated results. However, because the initial bead morphology in the model was designed close to the experimental data, and the constants were adjusted to make sure little fused surrounding material, this deviation is small. The weld residual stresses were calculated based on the thermal results.

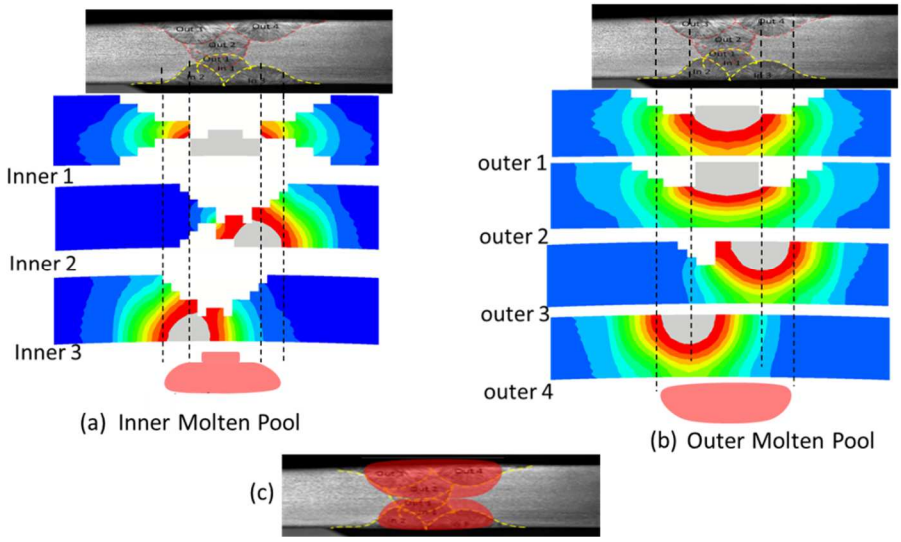

Fig. 5. Temperature contours of individual weld pass in the longitudinal welds: (a) inner passes, (b) outer passes, and (c) comparison of fusion boundary between simulation and experimental observation.

3.2 Residual Stress-Comparison of FEA with measurement

Fig. 6 summarizes the residual stress profiles as a function of depth in circumferential weld centerline and HAZ (~4mm away from weld toe on the outer surface) obtained from FEA and deep-hole drilling (DHD) measurement, which demonstrates a good agreement. Note that the experimental residual stress data close to the surfaces (≤2mm) were obtained from conventional hole drilling method. Through-wall high hoop tensile stress was observed in the circumferential welds. The maximum hoop stresses in circumferential welds are about 310MPa in the weld centerline and 240MPa in HAZ, respectively. The pre-existing residual stress in the base metal (up to 50MPa indicated by the DHD measurements) induced by the rolling process during manufacturing which was not considered in FE model, may lead to the difference in residual stress values near surfaces between experimental and simulation results. Moreover, in Fig. 6(a), the axial stress distribution from FEA has the trend to reach a force

balance condition, while the experimental results couldn't. For the longitudinal welds (not shown here), high tensile axial stress is present through thickness in the weld and HAZ. Besides, the maximum axial stresses are around 420MPa and 220MPa for weld centerline and HAZ, respectively.

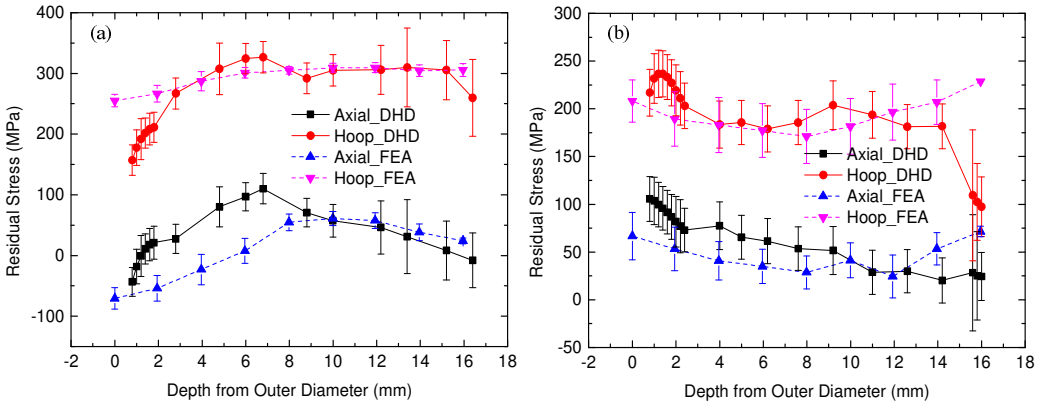

Fig. 6. Residual stress profiles as a function of depth in (a) weld centerline and (b) HAZ of circumferential weld from FE simulation (dashed lines) and DHD measurements (solid lines). The data of FE simulation is averaged from ten points in the steady state location.

The cross-section stress contour is extracted from FEA results, and compared with the results from contour method for both circumferential and longitudinal weld. Fig. 7 demonstrates the comparison of circumferential weld. Good agreement was achieved between the FEA and contour measurement results. Note that for the experimental contour measurement, the data appears noisy and scattered, which is possibly caused by the cutting-induced plasticity, surface contour measuring method, and the data processing algorithm [14,23,24]. The tensile stress region extends approximately 50mm away from the center of fusion zone on the outer (top) surface based on the experimental measurement. In comparison, this tensile stress region is slightly wider in FE simulation, which is in better agreement with the experimentally observed fusion boundary morphology as illustrated in Fig. 5. The longitudinal weld (not shown here) can also result in the through-wall tensile stress near the weld centerline. The tensile stress region extends approximately 25~30mm away from the center of fusion zone for longitudinal weld case. For the intersection area of the circumferential and longitudinal welds, similar trend was obtained.

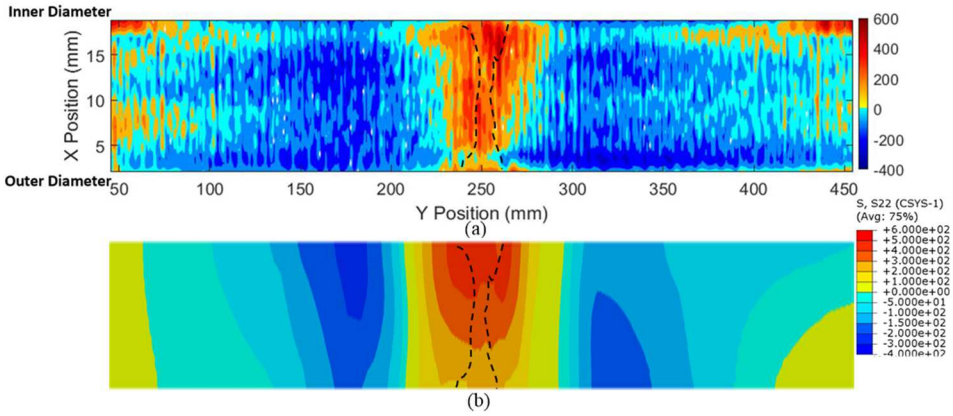

Fig. 7. Cross-sectional hoop stress maps for circumferential weld from (a) contour method and (b) FE model. The dashed lines outline the approximate fusion boundary characterized from the experiment.

3.3 Microstructures

Fig. 8 shows the typical SEM image of the microstructure in the region close to the fusion line. There is an obvious dendritic structure presenting in the fusion zone. These dendrites grow directionally. For the HAZ close to the fusion line, due to limited temperature, we can hardly observe any dendritic structure. To figure out the phase information for these dendritic structures, EBSD test was conducted in different zones. Fig. 9 gives the IPF map and phase map in the three regions (green=austenite and red=ferrite or martensite). It is clearly seen that the dendric structure in the weld metal is austenite, and the interdendritic phase is ferrite, as also demonstrated by other studies [25-27]. During the cooling process, the primary δ-ferrite is generated from the solidification at high temperature, and then the transformation from δ-ferrite to γ-austenite happens with the decrease of the temperature. The transformation from δ to γ is diffusion controlled, which cannot be wholly completed during the fast cooling process. So that some amount of δ-ferrite is retained. For the base metal, the EBSD phase map shows that there is small amount of δ-ferrite/α'-martensite existing (ferrite cannot be easily distinguished from martensite by EBSD method). It was reported that there may be small amount of residual δ-ferrite existed in the commercial austenitic stainless steel base metal [28]. Meanwhile, the rolling and cold forming process of the mockup canister would result in some content of α'-martensite [27, 29]. While from the morphology and location distribution, the bcc phase in base metal is mainly α'-martensite. For the HAZ, it is hard to find any phase besides the fcc austenite. The HAZ results were obtained from the region corresponding to a maximum temperature at around 900°C (the derivation of the temperature will be discussed later), which means under this temperature, the α'-martensite in the base metal was reversed to γ-austenite. The phase fraction for each region is given in Table 3, which depicts the existence of δ-ferrite and δ-ferrite/α'-martensite in weld metal and base metal, respectively, and also the reversion of α'-martensite in the HAZ. The IPF map results show that the ferrite and martensite are highly oriented. This crystallographic orientation can alter the mechanical/physical properties of the materials, and change the corrosion potential as well [30].

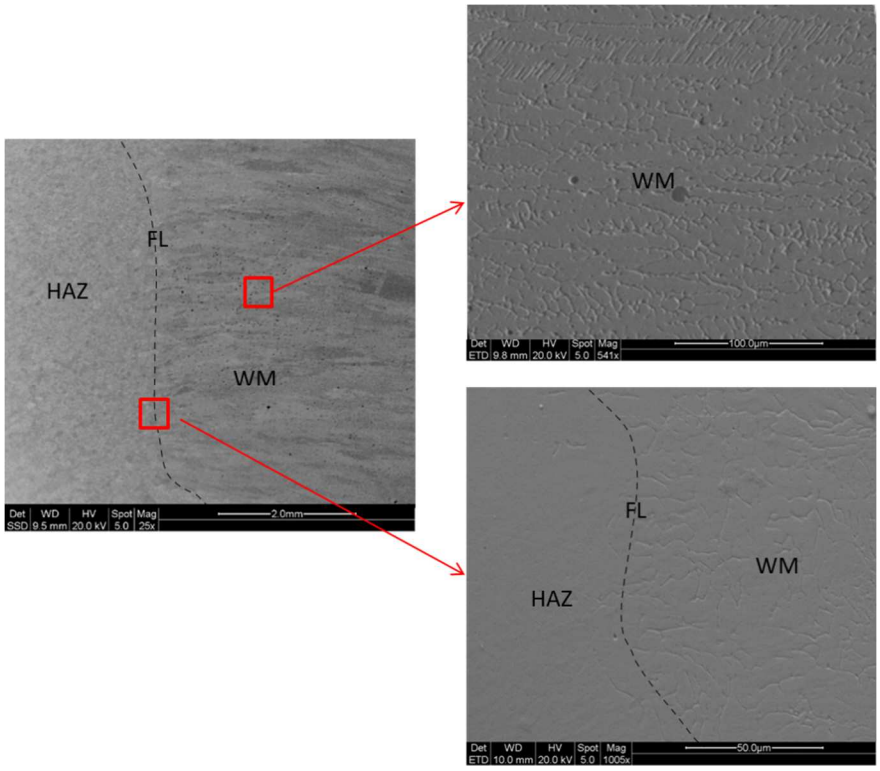

Fig. 8. SEM images showing the microstructure in the WM and HAZ. The dashed line represents the fusion line (FL)

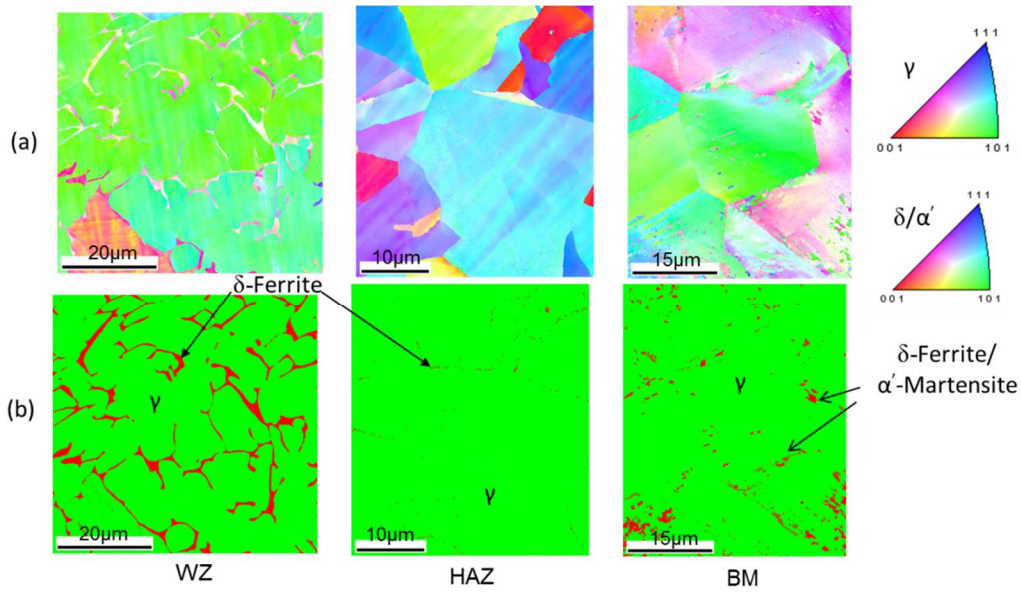

Fig. 9. EBSD results for different regions. (a) Inverse pole figures (IPF) map and (b) phase map

Table 3 Phase fraction from EBSD test

Phase	WZ	HAZ	BM
Ferrite (δ)	8.1%	0.2%	3.3% (δ-Ferrite + α′-Martensite)
Austenite (γ)	91.9%	99.8%	96.7%

The EBSD test shows a ferrite transformation in the weld metal and martensite reversion

in the HAZ. The magnetizable structures (δ-ferrite and α'-martensite) were also detected using Feritscope and the results were given in Fig. 10(a). The corresponding temperature profiles from the weld centerline to the base metal for circumferential and longitudinal welds were calculated through thermal simulation and plotted in Fig. 10(b) and Fig. 10(c). From Fig. 10(a), it is seen that the ferromagnetic number in the weld metal is large (above 10) due to the large amount of residual δ-ferrite in the fusion zone. While the ferromagnetic number is around 0.4-0.5 in the base metal, and around 0.2-0.3 in the HAZ. It indicates that the ferromagnetic number in the HAZ is a little lower than the base metal, which corresponds to the martensite reversion phenomenon revealed by EBSD test. The Feritscope test is a relative measure which bases on the volumetric measurement, while the EBSD technique is based on the area fraction. Therefore, they are not directly comparable with each other, but both can predict similar trend for different regions. There is an obvious low ferromagnetic number band existing in the HAZ, which is the martensite reversion region. From literature [31-33], we know that martensite reversion happens under certain temperature range. To determine the reversion temperature, the temperature profiles from the weld centerline to the base metal were then plotted for the longitudinal and circumferential weld through thermal simulation. For each node from the weld to the base metal in the FE model, temperature history is exported during the multi-pass welding process, and then the maximum temperature during the whole welding process is extracted. The temperature profile in Fig. 10(b) and Fig. 10(c) is actually the maximum temperature each node has experienced during the welding process. Fig. 11 gives an example that how the temperature history looks like for one node, through which the maximum temperature was extracted based on the eight peaks. Maximum temperature is extracted for each site along line L to get the temperature profiles. From Fig. 10, it can be found that the low ferromagnetic number region corresponds to a temperature range from around 400C° to 1500C°. Here 1500C° is the melting point used for the simulation. Thus a martensite reversion temperature as 400C° can be determined from the circumferential weld test data, which is similar to the reported value [31]. For the longitudinal weld, there is a narrow low ferromagnetic number region and a wide high ferromagnetic number region nearby. The high ferromagnetic number region was generated due to the effect of press brake during the cold forming process. For the sample from inner diameter of the mockup canister, similar conclusion can be drawn.

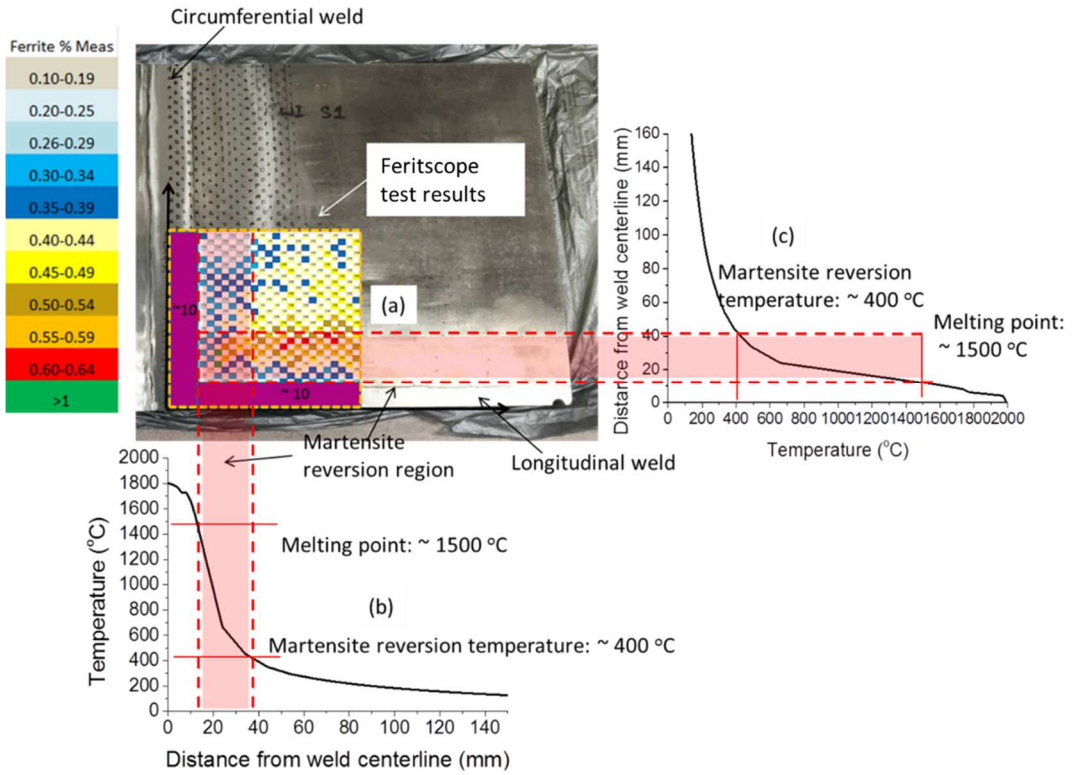

Fig. 10. Martensite reversion determined from Feritscope test and thermal simulation for outside part of the mockup canister. (a) Outside part of the mockup and the Feritscope test result, (b) maximum temperature profile from the center of circumferential weld to the base metal, (c) maximum temperature profile from the center of longitudinal weld to the base metal.

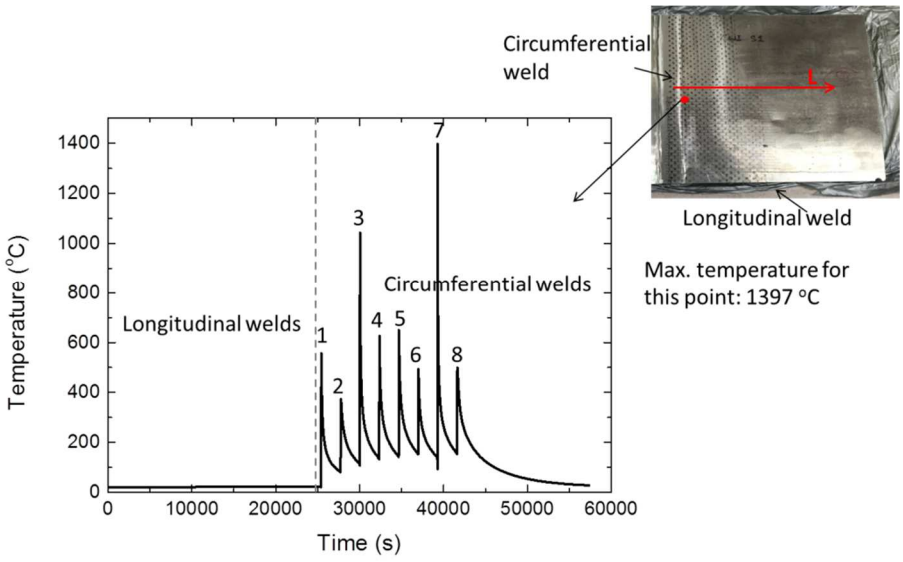

Fig. 11. Temperature history for one point located in HAZ.

The manufacturing procedures of the SNF canister include the pinch/bump forming process of the plate to make a cylinder and the following welding process to join the edges of a cylinder or join different cylinders. The pinch/bump forming process would induce large deformation to the plates, and the welding process would induce thermal impact and residual stresses to the material adjacent to the weld. The ferrite content shown in Fig. 12 is a result of

the combined effect from the three factors, i.e., large deformation, thermal impact and residual stresses. To figure out the underlying mechanism of the Feritscope data in Fig. 12, a physical simulation procedure was employed to model the mechanical and thermal history experienced by the canister weldment. A cold work process by reduction of the thickness of the 304 SS plate by 16.5% was applied first to represent the pinch forming. Then a sensitization process through heat treating the plate was applied to represent the weld thermal impact. With that, a cold work process again by reduction of the thickness of the 304 SS plate by 16.5% was applied to represent the weld residual stress. After the specimen was made, Feritscope was used to measure the ferrite content in it. Besides the specimen under this making procedure, three other specimens were also prepared to investigate the influence of each step on the final ferrite content distribution. The steps used in the other three procedures were indicated in Fig. 13, and the Feritscope measurement data for all the four procedures was also given in Fig. 13.

As it can be seen in Fig. 13, the initial ferrite content in the specimen is low, and the cold working would lead to a little increase to the ferrite content, while the heat treatment would induce a small reduction to the ferrite number. However, the cold work after the heat treatment process would significantly increase the ferrite content (more than 1700%). If without the first step cold work, the cold work after the heat treatment process could only induce a relative low increase of the ferrite (500%). As it is known that cold work would induce extensive dislocation networks and the generation of martensite [27, 29, 34], during the heat treatment of the cold worked 304 SS at low temperature, a high density of fine carbides would form quickly both along the grain boundaries as well as along the slip bands within the grains [35, 36]. The cold work after the heat-treated samples would lead to tremendously increase of the dislocations, and meanwhile, these dislocations could be pinned by the high density of fine chromium carbides generated during the heat treatment step. So the high density of dislocations pile up around the chromium carbides, which promotes the formation of large amount of martensite [37], as indicated by the magnetic number. For the specimen without the first cold work step, a relative small amount of chromium carbides were generated along the grain boundaries, which could only pin a small amount of dislocations, resulting in relative low martensite content. During the manufacturing procedure of the canister, the pinch forming process induce the contact between the press brake and the plate, as shown in Fig.12, which can be called the first cold working region. The welding procedure could induce thermal impact (heat treatment) and residual stresses (second cold working region). As explained previously, the combination of the three factors would result in the generation of high amount of martensite, so there are belts with high values of magnetic number corresponding to these contacted areas, which could be clearly seen in Fig. 12.

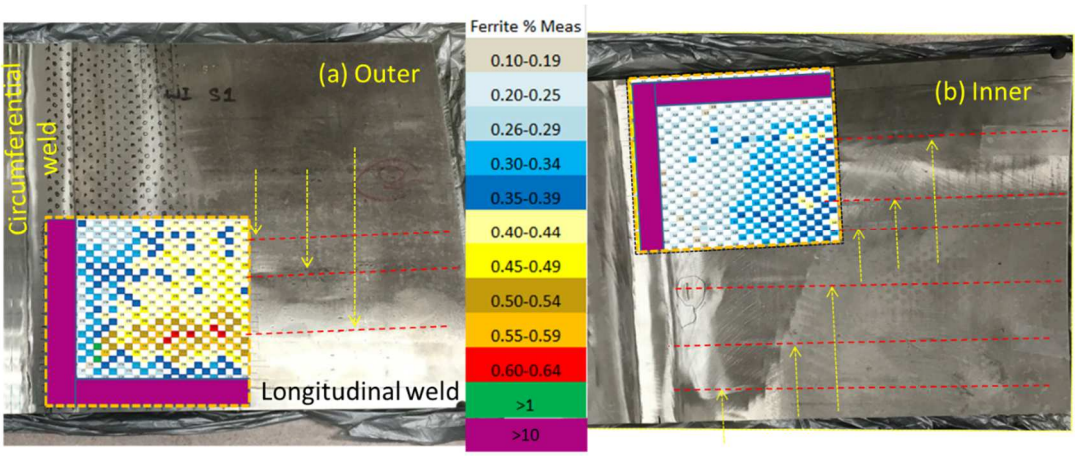

Fig. 12. Ferrite content distribution for (a) outer and (b) inner sides of the canister weldment under the combined effects of cold working and welding. The yellow arrows and the red lines are used to indicate the locations where the press brake made contact to the plate for pinch forming step. The corresponding Feritscope testing data for the contacted area could be obtained by referring to the location of the red lines

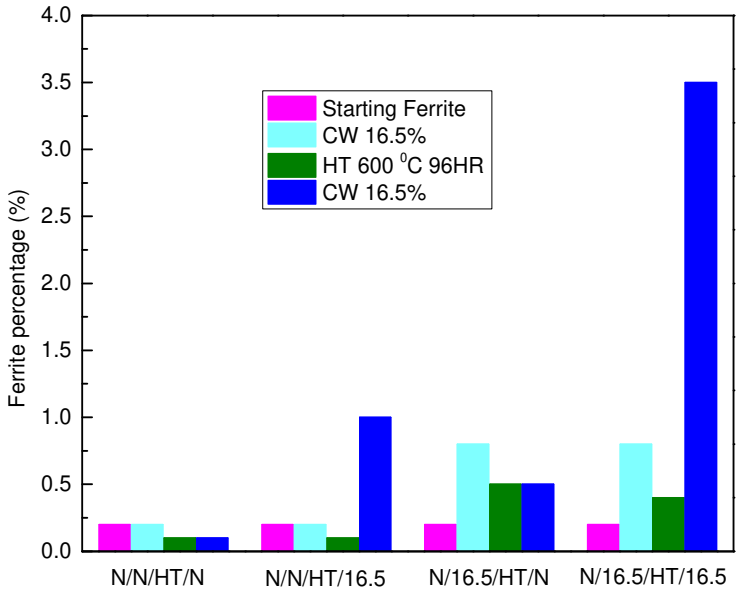

Fig. 13. The change of ferrite content under different physical simulation procedures. The "N" represents no actions, "HT" represents heat treat at 600^{0}C, 960 hours, "16.5" represents cold work by reduction the thickness

The inclusion distribution in different regions was detected using optical microscopy, and the element compositions were characterized by EDS method. Fig. 14 shows the distribution of inclusions in different regions. It was found that for the base metal and HAZ, there are a few elongated inclusions. While for the weld metal, there are a lot of spherical inclusions. The typical size of the inclusions is below 2μm. Meanwhile, the inclusion distribution in weld metal presents obvious pattern character, which is related to the underlying dendritic structure (the sample is not etched here, so the dendritic structure is not easily seen). To uncover the element composition of these inclusions, the EDS characterizations were adopted for the inclusions in different zones, as shown in Fig. 15. For each region, at least 10 spot scanning tests were conducted, and the results are similar.

Because the size of the inclusions is small, and the EDS gives an average value in a certain area (around 1μm), the EDS spectrums for the inclusion include some of the information from the matrix.

As shown in Fig. 15(a-b), for the elements constitutions in matrix there is a higher content of Cr and lower content of Ni for the δ matrix, which corresponds to the feature of vermicular ferrite. For the inclusions in the base metal (Fig. 15(c)), there is an obvious increase for the atomic percent of the Mn (from 1.62 to 3.44) and S (from 0.35 to 3.08) element. Meanwhile, the atomic ratio between Mn and S is close to 1 (3.44:3.08) for the inclusions, so we can conclude that the elongated inclusions for the base metal are MnS. For the HAZ (Fig. 15(d)), there is also an obvious increase for the atomic percent of the Mn (from 1.62 to 5.69) and S (from 0.35 to 4.98), and the atomic ratio between Mn and S for the inclusion is close to 1 (5.69:4.98). Thus the inclusions for the HAZ are also MnS. We couldn't find any carbide in the HAZ using EDS test, probably due to the low carbon feature of the material. For the weld metal (Fig. 15(e)), there is an obvious increase for the atomic percent of the O (from 12.65 (γ), 14.34 (δ) to 41.46), Si (from 1.02 (γ), 1.12 (δ) to 14.46) and Mn (from 1.62 (γ), 1.41 (δ) to 14.2), which reveals the inclusions for the weld metal are mainly $(Mn,Si)_xO_y$. The inclusions can serve as the ferrite nucleation sites in the weld, like these oxide inclusions, and also they can be the pitting initiation sites under corrosion environment, like the MnS inclusions. Thus, the inclusions have large impact on the mechanical and corrosion properties of the materials.

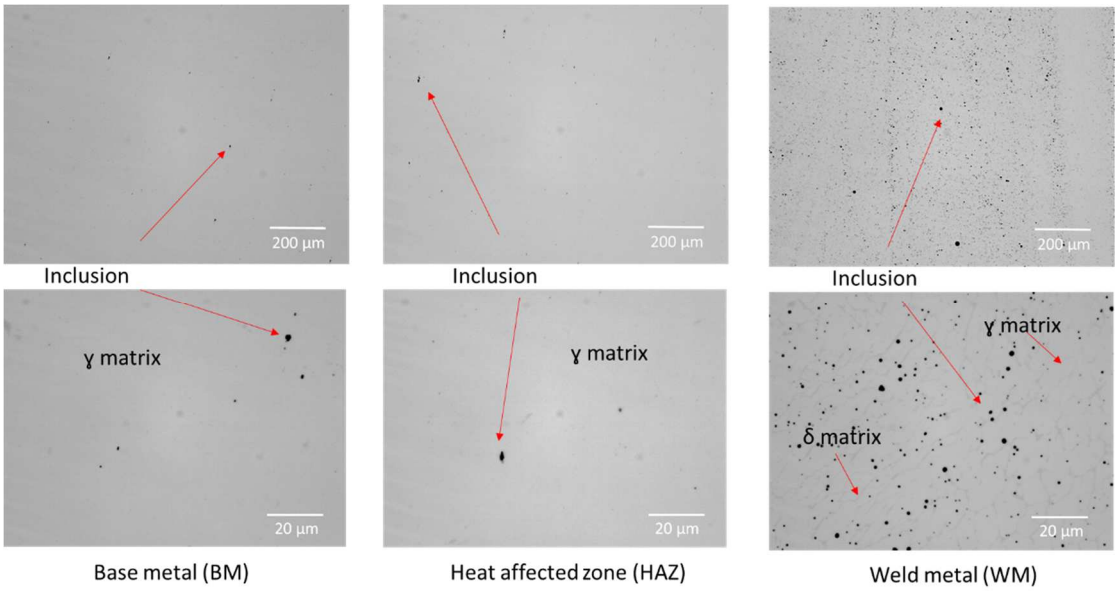

Fig. 14. Inclusions distribution in different zones

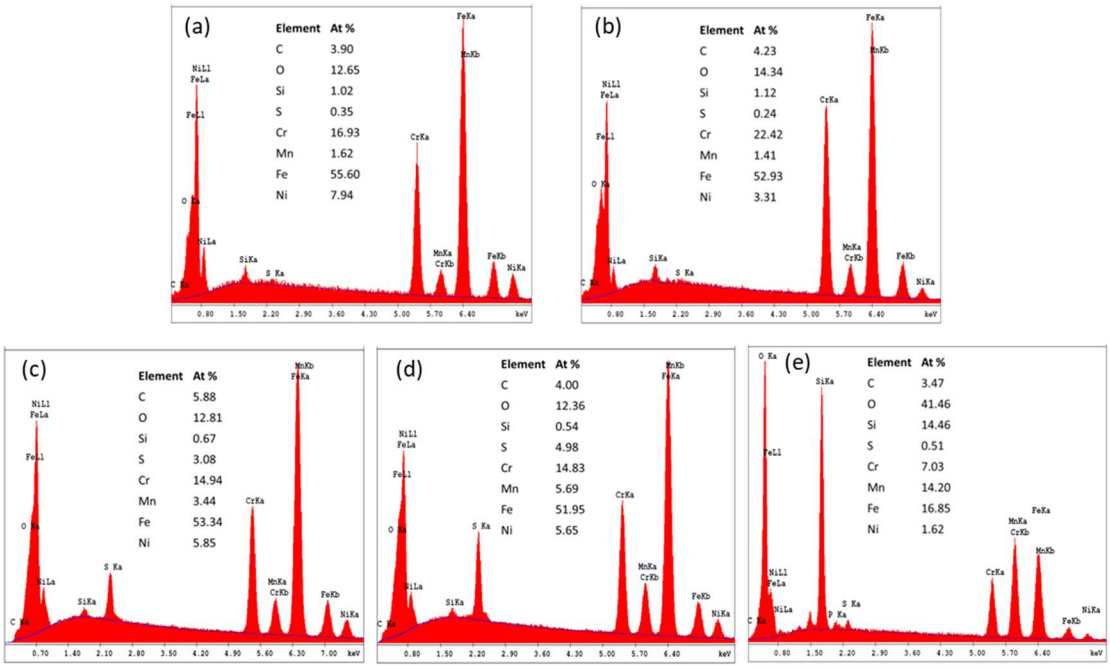

Fig. 15. Typical EDS characterization data of (a) γ matrix, (b) δ matrix, (c) inclusions in BM, (d) inclusions in HAZ and (e) inclusions in WM. The inserted tables indicate the atomic percentage of the elements for each spectrum

4. Discussions

Through the FEA and experimental measurement, a through-wall high tensile stress was predicted in the region close to the weld centerline in both longitudinal and circumferential weld for the mockup canister. The typical tensile stress along the weld direction is above the yield point in the fusion zone and close to the yield point in the HAZ. This tensile stress could offer the stress condition for the CISCC to happen. As discussed in literature [38], the degradation caused by pitting is low, while the existence of residual stress could obviously accelerate the degradation rate. Also, the magnitude of the stress and the type of stress (tensile or compressive) could induce different SCC behaviors. It was demonstrated that the threshold tensile stress of the SCC could be as low as $0.5*\sigma_y$ (yield point) for solution annealed type 304/304L SS, and even smaller than $0.25*\sigma_y$ for sensitized type 304 SS under certain corrosion environment [39]. While the residual compressive stress could bring significant suppression of the SCC susceptibility [40]. Therefore, both the longitudinal and circumferential weld residual stress results suggest that a potential CISCC indication would have a tendency to grow along the canister thickness direction. The through-wall high tensile stress in and near the weld would have deleterious effects on the potential crack growth since no compressive stress could slow down or arrest the through-wall growth.

As for the microstructure, the existence of δ-ferrite, α'-martensite, inclusions in different regions could offer as the initiation sites for the pitting to happen in the 304/304L canister. The strain-induced martensite in 304L SS could present high SCC susceptibility behavior as compared with the solution-annealed sample [18]. According to the previous studies [41], the corrosion resistance of martensite is lower than that of austenite. The pinch forming process could induce the formation of high amount of martensite, as well as increase of the kinetics of

sensitization in the contacting region, which needs to receive more attention for the future detection. Also, the mixed austenite/ferrite in the skeletal weld metal structures could result in galvanic corrosion in the corrosive environment. Besides, the different crystallographic orientations may also result in different corrosion potentials, which will be the topic of our following research. Sulfides are generally detrimental to pitting resistance and crevice corrosion resistance [38]. As there are some sulfide inclusions in the base metal and HAZ, which could act as initiation sites for pits and stress corrosion cracks, the susceptibility of CISCC would increase.

Since it's extremely difficult to do the CISCC test on site, it is needed to design a test setup in the lab to reflect the corrosion behavior of the actual canister. Based on the conditions of the mockup canister, we are working on designing a four-point bend structure to duplicate the weld residual stress level and microstructure condition on a real canister. Through this four-point bend test, the influence of different stress conditions on the corrosion behavior can be considered in one sample. And the effect of the surface roughness, sensitization, δ-ferrite/α'-martensite, crystallographic orientation, texture, inclusions on the potential pitting initiation and growth rate will be taken into consideration. The corrosive environment will be simulated by a corrosion chamber, for which the temperature, relative humidity and salt load will be considered as the main influence factors. The results in this study could offer useful information for the designing of the four-point bend sample and the corrosion test.

5. Conclusions

This paper analyzed the weld residual stresses and microstructure of the mockup canister for spent nuclear fuel, aiming at providing important information for the prediction of CISCC. The following conclusions can be derived:

(1) Welding-induced residual stresses from FE simulation were in good agreement with the experimental measurement results. Through-wall high tensile hoop stresses were observed in both the fusion zone and HAZ in circumferential welds, with a maximum value of about 310MPa. In comparison, through-wall high axial stresses were observed in the fusion zone and HAZ in longitudinal welds, with a maximum value of 420MPa.

(2) For the weld metal, the microstructure is composed of δ-ferrite and γ-austenite phase, which present as dendritic structure. For the base metal, there is α'-martensite initiated during the rolling process of the plate. Both the EBSD technique and Feritscope test show that the α'-martensite could be reversed to γ-austenite in the HAZ. There are a few elongated MnS inclusions existing in the base metal and HAZ, and a lot of spherical $(Mn,Si)_xO_y$ inclusions existing in the weld metal, with a size normally smaller than 2μm.

(3) A martensite reversion temperature as of 400C° was predicted from the combination of thermal simulation and Feritscope test.

Acknowledgement

This work was supported by the DOE, Nuclear Engineering University Program (NEUP)

under grand number DE-NE0008442 of Integrated Research Program (IRP), no. IRP-15-9318.

References

[1] J. Tani, M. Mayuzumi, N. Hara, Journal of Nuclear Materials 379 (2008) 42-47.
[2] R. M. Kain, Materials Performance 29 (1990) 60-62.
[3] USNRC, NRC Information Notice 2012-20, Office of Nuclear Material Safety and Safeguards, Washington, DC, 2012.
[4] D. G. Enos, C. R. Bryan, K. M. Norman, FCRD-UFD-2013-000324. U. S. Department of Energy, Office of Used Nuclear Fuel Disposition, 2013.
[5] C. R. Bryan, D. Enos, SAND2014-16383, Sandia National Laboratories, 2014.
[6] C. R. Bryan, D. G. Enos, SAND2015-1746, Sandia National Laboratories, 2015.
[7] Y. Wan, W. Jiang, J. Li, G. Sun, D. Kim, W. Woo, S. Tu, Materials Science and Engineering: A 699 (2017) 62-70.
[8] W. Jiang, W. Chen, W. Woo, S. Tu, X. Zhang, V. Em, Materials & Design 147 (2018) 65-79.
[9] W. Jiang, W. Woo, Y. Wan, Y. Luo, X. Xie, S. Tu, J. Pressure Vessel Technol. 139 (2017) 031401.
[10] Y. Wang, G. Li, S. Chen, Journal of Constructional Steel Research 76 (2012) 93-99.
[11] A. Kosaki, Nuclear Engineering and Design 238 (2008) 1233-1240.
[12] NRC, ADAMS ML13330A512, NRC Technical Letter Report, 37, Washington, D.C. 2013.
[13] J. J. Wang, A. Payzant, J. Bunn, K. An, ORNL/TM-2018/827, Oak Ridge National Laboratory, 2018.
[14] D. G. Enos, C.R. Bryan, FCRD-UFD-2016-000064, SAND2016-12375 R, Sandia National Laboratories, 2016.
[15] S. Chatzidakis, W. Tang, J. Chen, R. Miller, A. Payzant, J. Bunn, J. Wang, IHLRWM2019, Knoxville, TN, April 14-18, 2019.
[16] L. Hackel, J. Rankin, M. Walter, C. B. Dane, W. Neuman, P. Oneid, G. Thomas, F. Bidrawn, Procedia Structural Integrity 19 (2019) 346-361.
[17] M. Koshiishi, H. Fujimori, M. Okada, A. Hirano, Hitachi Review 58 (2009) 88-93.
[18] S. Ghosh, V. Kain, Journal of nuclear materials 403 (2010) 62-67.
[19] Standard: DIN 32514-1, Determination of ferrite number of austenitic weld metal measurement method, Dusseldorf, Germany, 1990.
[20] D. Deng, H. Murakawa, Computational Materials Science 37 (2006) 269-277.
[21] C. Liu, J. X. Zhang, C. B. Xue, Fusion Engineering and Design 86 (2011) 288-295.
[22] J. Goldak, A. Chakravarti, M. Bibby, Metallurgical Transactions B 15 (1984) 299-305.
[23] M. B. Prime, R. J. Sebring, J. M. Edwards, D. J. Hughes, P. J. Webster, Experimental Mechanics 44 (2004) 176-184.
[24] Y. L. Sun, M. J. Roy, A. N. Vasileiou, M. C. Smith, J. A. Francis, F. Hosseinzadeh, Experimental Mechanics 57 (2017) 719-734.
[25] R. Unnikrishnan, K. S. N. Satish Idury, T. P. Ismail, A. Bhadauria, S. K. Shekhawat, R. K. Khatirkar, S. G. Sapate, Materials Characterization 93 (2014) 10-23.

[26] G. R. Mirshekari, E. Tavakoli, M. Atapour, B. Sadeghian, Materials and Design 55 (2014) 905-911.
[27] J. B. Cai, C. Yu, R. K. Shiue, L. W. Tsay, Journal of Nuclear Materials 465 (2015) 774-783.
[28] I. R. Souza Filho, M. J. R. Sandim, R. Cohen, L. C. C. M. Nagamine, J. Hoffmann, R. E. Bolmaro, H. R. Z. Sandim, Journal of Magnetism and Magnetic Materials 419 (2016) 156–165.
[29] L. W. Tsay, Y. J. Lin, C. Chen, Corrosion Science 63 (2012) 267-274.
[30] A. Shahryari, J. A. Szpunar, S. Omanovic, Corrosion Science 51 (2009) 677-682.
[31] J. Singh, Journal of materials science 20 (1985) 3157-3166.
[32] K. Mumtaz, S. Takahashi, J. Echigoya, Y. Kamada, LF. Zhang, H. Kikuchi, K. Ara, M. Sato, Journal of materials science 39 (2004) 1997-2010.
[33] S. S. M. Tavares, D. Fruchart, S. Miraglia, Journal of Alloys and Compounds 307 (2000) 311-317.
[34] P. G. Shewmon, Diffusion in Solids, P. 175, McGraw-Hill, New York, 1963.
[35] E. C. Bain, R. H. Aborn, J. J. B. Rutherford, Trans. Amer. Soc. Steel Treating 21 (1933) 481-509.
[36] C. L. Briant, A. M. Ritter, Metallurgical Transactions A 11 (1980) 2009-2017.
[37] J. Liu, C. Chen, Q. Feng, X. Fang, H. Wang, F. Liu, J. Lu, D. Raabe, Materials Science & Engineering A 703 (2017) 236-243.
[38] Y. Xie, J. Zhang, Journal of Nuclear Materials 466 (2015) 85-93.
[39] M. Mayuzumi, T. Arai, K. Hide, Zairyo-to-Kankyo 52 (2003) 166-170.
[40] R. Sundar, P. Ganesh, B. S. Kumar, R. K. Gupta, D. C. Nagpure, R. Kaul, K. Ranganathan, K. S. Bindra, V. Kain, S. M. Oak, B. Singh, Journal of Materials Engineering and Performance 25 (2016) 3710-3724.
[41] J. Nakano, Y. Nemoto, T. Tsukada, T. Uchimoto, Journal of Nuclear Materials 417 (2011) 883-886.